Journal of Computational Applied Mechanics 2022, 53(2): 282-296

DOI: 10.22059/JCAMECH.2022.341232.707

RESEARCH PAPER

Numerical simulation of the mixing layer problem based on a new two-fluid turbulence model

Zafar Mamatkulovich Malikov [1], Akmal Axadovich Mirzoev[2], Murodil Erkinjon Ugli Madaliev [3,*]

[1] *AKFA University, 10, 1-blind alley, Kukcha Darvoza, Tashkent, 100020, Uzbekistan*
[2] *Institute of Mechanics and Seismic Stability of Structures, Academy of Sciences of the Republic of Uzbekistan*
[3] *Fergana Polytechnic Institute, 86, st. Fergana, Fergana, 150107, Uzbekistan*

Abstract

The paper considers the modeling of a layer of mixing of two flows with different velocities in a flat channel. The calculations are based on the numerical solution of the system of non-stationary equations of the two-fluid turbulence model. The results of longitudinal velocity and turbulent stress profiles in different sections of the channel are obtained. For the numerical implementation of the equations of turbulent hydrodynamics, the control volume method was used, and the relationship between velocities and pressure was found using the SIMPLE procedure. In this case, the convective terms in the equations were approximated by the difference against the flow in an explicit form with a second-order accuracy, and the diffusion terms by the central difference in an implicit form. To confirm the correctness of the obtained numerical results, a comparison was made with experimental data from the NASA database.

Keywords: Navier–Stokes equations, two-fluid model, control volume method, turbulent stresses, SIMPLE method.

1. Introduction

Mixing layers are formed between parallel streams at different velocities. They are often found both in nature and in various technical devices. In nature, one can observe the mixing of two oceanic streams, while in technology, mixing occurs in jet streams. This phenomenon is also relevant in medicine. For example, studies [1-3] investigate the distribution of drugs when injected into the abdominal cavity for the treatment of cancer.

Mixing layers also form between air and nanomaterials in many microelectromechanical systems. In recent years, piezoelectric nanostructures such as ZnO nanowires, GaN nanorods, BaTiO thin films, and PZT nanofibers have received much attention due to their excellent mechanical and electronic properties. In Ref. [4], potential applications of systems of piezoelectric nanostructures (PNF) and double piezoelectric nanostructures (DPNF) as nanoelectromechanical mass sensors are considered. In Ref. [5], a nonlocal continuum model of a plate was developed for transverse vibration of a system of double piezoelectric nanoplates (DPNPS) with an initial stress under the action of an external electric voltage. The Pasternak foundation model is used to account for the shear effect between two piezoelectric nanoplates in combination with the normal behavior of the binding elastic medium. In Ref. [6], a nonlinear continuum model of large-amplitude oscillations of nanoelectromechanical resonators was developed using piezoelectric nanostructures (PNF) under the action of an external electric voltage.

Recently, graphene sheets have shown significant potential for environmental engineering applications such as wastewater treatment. In Ref. [7], the reaction to warpage of an orthotropic single-layer graphene sheet (SLGS) is studied in an analytical form in a closed form using the non-local Ehringen theory. It is well known that rotating

* Madaliev Murodil. Tel.: +98943989896.
E-mail address: sMadaliev.ME2019@mail.ru, m.e.madaliyev@ferpi.uz

nanobeams can have different dynamic and stable responses to different types of loads. In the study [8], attention is focused on studying the influence of the magnetic field, surface energy, and compressive axial load on the dynamic and stable behavior of nanobeams. Using the nonlocal theory of elasticity, the influence of a small scale on the axial vibrations of a conical nanorod is studied. The theory of nonlocal elasticity is used to analyze the mechanical behavior of nanosized materials [4-37].

The article [30] presents a study of the buckling characteristics of nanosized rectangular plates under biaxial compression, taking into account thickness non-uniformity. Constitutive differential equations are derived on the basis of nonlocal continuum mechanics. Numerical solutions for buckling loads are obtained using the Galerkin method. In Refs. [10, 15], a non-local continuum model of nonlinear free oscillations of size-dependent magnetoelectroelastic nanoplates under the action of external electric and magnetic potentials was developed. The article [20] presents a new explicit formula for the length-dependent persistent length of microtubules, taking into account surface effects. In addition, surface effects on the bending characteristics of microtubule systems in the viscoelastic surrounding cytoplasm are investigated using a modified Timoshenko bundle model.

Piezoelectric nanomaterials such as zinc oxide (ZnO) are low toxic and have many biomedical applications including optical imaging, drug delivery, biosensors, and biomechanical energy harvesting using hybrid nanogenerators. In Ref. [14], vibration, warping, and intelligent control of microtubules (MT) embedded in an elastic medium in a thermal medium using a piezoelectric nanoshell (PNS) are studied. The buckling response of an orthotropic single layer graphene sheet (SLGS) is investigated using the theory of non-local elasticity. Linearly changing normal stresses act on two opposite edges of the plate. Small scale effects are taken into account. To derive the basic equations, the nonlocal Ehringen theory and the equilibrium equations of a rectangular plate are used [31].

In Ref. [16], a new size-dependent plate model was developed based on a higher-order non-local strain gradient theory. The influence of higher-order deformations in combination with non-local effects of higher and lower orders is taken into account. The presence of three different types of scale parameters in the formulation leads to a theory that is able to take into account both a decrease and an increase in the rigidity of structures at the nanolevel. The basic differential equations for the loss of stability of nanoplates resting on a two-parameter elastic foundation are derived using the principle of virtual work. In Refs. [17, 22], a model of a plate with a nonlocal higher-order strain gradient was developed for vibration of piezoelectric nanofilms (PNF) as nanoelectromechanical mass sensors. PNF, carrying many nanoparticles in any places, is subjected to thermoelectromechanical loads.

In Ref. [23], the behavior of free vibrations of a rectangular graphene sheet under a shearing plane load is studied. The theory of non-local elasticity has been implemented to study the vibration analysis of orthotropic single layer graphene sheets (SLGS) subjected to in-plane shear loading. Using the principle of virtual work, the basic equations for rectangular nanoplates are derived. In Ref. [24], the nonlocal theory of elasticity was implemented to study the shear buckling of orthotropic single-layer graphene sheets (SLGS) in a thermal medium.

In Ref. [28], the behavior of free vibrations of a round and annular graphene sheet is studied. Using the non-local theory of elasticity, the basic equations for single-layer graphene sheets (SLGS) are derived, and the non-local parameter is included in the arguments of the Bessel functions.

In Ref. [29], the behavior of free vibration of a round graphene sheet under a preload in the plane is studied. Using the theory of non-local elasticity and the theory of Kirchhoff plates, the basic equation is derived for single-layer graphene sheets (SLGS).

Based on the nonlocal theory of elasticity of the strain gradient, the nonlinear free and forced oscillatory behavior of a porous functionally graded Euler-Bernoulli nanobeam [12] subjected to mechanical and electrical loads was studied. It is assumed that the porous functionally graded (FG) nanobeam rests on a nonlinear foundation. In addition, it is assumed that the material properties of the nanobeam change in the thickness direction.

In Ref. [25], the effect of temperature change on the oscillation frequency of a single-layer graphene sheet immersed in an elastic medium is studied. Using the non-local theory of elasticity, the basic equations for single-layer graphene sheets are derived. Using the Levy and Navier solutions, analytical frequency equations for single-layer graphene sheets are obtained.

The study [11] investigates the nonlinear vibrational analysis of new generation nanostructures. The composite nanoplate is made from a functional grade (FG) core and two lipid layers on top and bottom of the FG core as face sheets. A nonlinear analysis of vibration in the presence of an external harmonic excitation force is investigated. The effect of porosity on the analysis of free and force vibrations of a composite nanoplate has been studied.

In Refs. [18, 35], the vibrational behavior of a rotating viscoelastic nanobeam embedded in a visco-Pasternak foundation was studied. The main equation is obtained using the theory of surface elasticity and non-local theory of elasticity. The influence of humidity on the oscillation frequencies of a viscoelastic nanobeam in a thermal medium has been studied.

Back in the 19th century, the classics proved that tangential discontinuities are unstable, which lead to

turbulence. Therefore, this problem, despite its simplicity, is a rather difficult test problem for many turbulence models. It is known that at present there are many different semi-empirical models of turbulence. Despite their large number, there is still no universal turbulence model. Therefore, depending on the problem, one or another turbulence model is selected for numerical research. The NASA turbulence database [38, 39] provides a comparative analysis of various semi-empirical models. From this analysis, it can be concluded that the Spalart-Allmaras SA [40] and Menter SST [41] models have the highest rating. These models are highly rated because they are practical and capable of describing a wide range of turbulence problems with sufficiently high accuracy [42, 43].

Recently, the work of one of the authors of this article has been published, where a new turbulence model is proposed [44, 45]. The peculiarity of this model is that it is based on a new approach to the problem of turbulence. In this work, it is shown that a turbulent flow can be represented as a heterogeneous mixture of two fluids with different velocities. Therefore, the new model is named as the two-fluid turbulence model. The idea of representing a turbulent flow as a mixture of two fluids belongs to Spalding [46]. However, in Spalding's two-fluid model, additional equations were used to search for turbulent parameters, which were obtained on the basis of various hypotheses. As a result, the number of equations to be solved doubled compared to conventional RANS models. This circumstance led to the fact that soon this model lost its attractiveness and was not widely used. As regards the mentioned new two-fluid model, it is a closed system of equations and the theory of kinetics and the Prandtl hypothesis are used to determine the main parameters of turbulence. Therefore, additional empirical equations are not involved. In Refs. [44, 45], a new model was used to study the flow around a plate, a free turbulent jet, and a rotating flow. It is shown that the new two-fluid turbulence model has high accuracy, is simple for solving engineering problems, and is able to adequately describe anisotropic turbulence. The paper also compares the results of other well-known Spalart models – Allmaras SA [40], Menter SST [41], and Reynolds stresses SSG LRR-RSM [47]. Thus, the paper compares four models that belong to different classes. Menter's SST model is based on Kolmogorov's theory of the cascade transition of mechanical energy into turbulent energy. The Spalart-Allmaras SA model belongs to one-parameter models, where the transport equation for the modified turbulent viscosity is written. As for the Reynolds stress model SSG LRR-RSM, it does not use the Boussinesq hypothesis and writes its own equation for each turbulent stress tensor.

2. Setting the task

A new two-fluid model for turbulent mixing of two flows in a flat channel is being validated. In addition, a study of the influence of numerical schemes on the solution of the problem is carried out. Thus, along with studying the structure of the flow after mixing two flows, the goal is also to test the effectiveness of finite difference schemes for calculating complex flows. For this purpose, explicit and semi-implicit numerical schemes against the flow were used [48]. The obtained numerical results are compared with the experimental data from the NASA database [38].

The experiment uses a 3 mm thick separation plate in a 300 mm wide tunnel (Fig. 1). The end of the plate is located at the point x = 0, and two fluid flows with different speeds merge below this point. The plate is modeled with a taper starting at x = -50 mm and ending with a trailing edge thickness of 0.3 mm at x = 0. The channel length is x = 1800 mm. The speed of the upper flow is $U_1 = 41.54$ m/s and the lower flow is $U_2 = 22.4$ m/s. The Reynolds number calculated from L=1 mm and the upper flow velocity was equal to 2900. In the experiment, the upper high-speed flow has a boundary layer thickness at x=-10 mm (near the trailing edge of the plate) of about 9.6 mm and a pulse thickness of about 1 mm. The lower flow with a lower velocity has a boundary layer thickness of about 6.3 mm and a pulse thickness of about 0.73 mm [49].

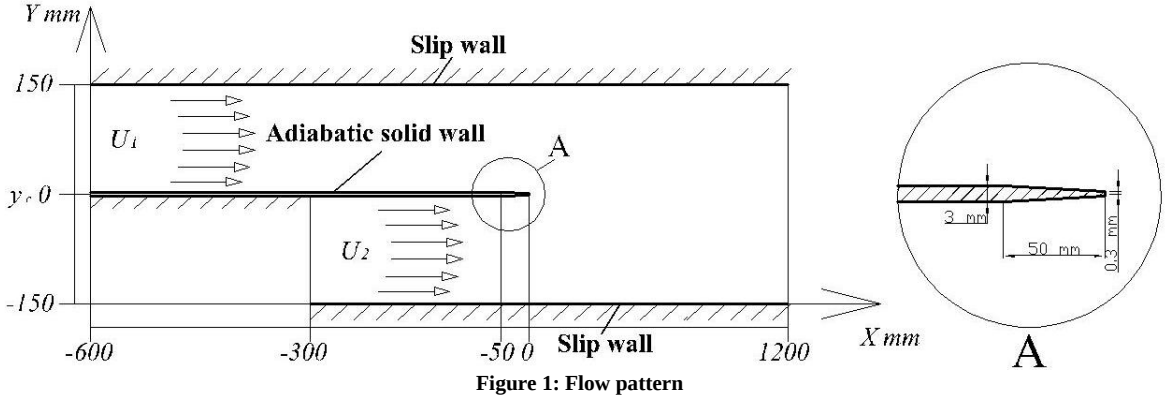

Figure 1: Flow pattern

3. Two-fluid turbulence model

The system of differential equations of the two-fluid turbulence model has the form [44]:

$$\begin{cases} \dfrac{\partial \overline{V_j}}{\partial x_j}=0, \\ \dfrac{\partial \overline{V_i}}{\partial t}+\overline{V_j}\dfrac{\partial \overline{V_i}}{\partial x_j}+\dfrac{\partial \overline{p}}{\rho \partial x_i}=\dfrac{\partial}{\partial x_j}\left[\nu\left(\dfrac{\partial \overline{V_i}}{\partial x_j}+\dfrac{\partial \overline{V_j}}{\partial x_i}\right)-\vartheta_j\vartheta_i\right], \\ \dfrac{\partial \vartheta_i}{\partial t}+\overline{V_j}\dfrac{\partial \vartheta_i}{\partial x_j}=-\vartheta_j\dfrac{\partial \overline{V_i}}{\partial x_j}+\dfrac{\partial}{\partial x_j}\left[\nu_{ji}\left(\dfrac{\partial \overline{V_i}}{\partial x_j}+\dfrac{\partial \overline{V_j}}{\partial x_i}\right)\right]+F_{si}+F_{fi}, \\ \nu_{ji}=3\nu+2\left|\dfrac{\vartheta_i\vartheta_j}{\mathrm{def}\,(\overline{\vec{V}})}\right| \quad i\neq j, \qquad \nu_{ii}=3\nu+\dfrac{1}{\mathrm{div}\,\vec{\vartheta}}\left|\dfrac{\vartheta_k\vartheta_k}{\mathrm{def}\,(\overline{\vec{V}})}\right|\dfrac{\partial \vartheta_k}{\partial x_k}, \\ \vec{F}_f=-K_f\vec{\vartheta}, \qquad \vec{F}_s=C_s\mathrm{rot}\overline{\vec{V}}\times\vec{\vartheta}. \end{cases} \tag{1}$$

In the system of equations (1) $\overline{V_i}$, ϑ_i is, respectively, the averaged and relative velocities of the turbulent flow, $\overline{p}$ is the averaged hydrostatic pressure, ν is the molecular kinematic viscosity, ν_{ji} is the effective molar viscosity, F_{si} is the transverse Saffmen force due to the shear velocity field, F_{fi} is the friction force, ρ density, $C_s=0.2$ empirical coefficient. The forces of interaction between two fluids arise as a result of the relative motion of fluids and are determined by the expressions:

$$\vec{F}_s=C_s\mathrm{rot}\overline{\vec{V}}\times\vec{\vartheta}, \qquad \vec{F}_i=-K_f\vec{\vartheta}, \tag{2}$$

where K_f is the coefficient of friction, which is determined by the expression:

$$K_f=C_1\lambda_{\max}+C_2\frac{\left|\vec{d}\cdot\vec{\vartheta}\right|}{d^2}. \tag{3}$$

Here d is the nearest distance to a solid wall, $\lambda_{\max}$ is the largest root of the characteristic equation:

$$\det(A-\lambda E)=0, \tag{4}$$

where A is the matrix:

$$A=\begin{vmatrix} -\dfrac{\partial \overline{V_1}}{\partial x_1} & -\dfrac{\partial \overline{V_1}}{\partial x_2}-C_s\zeta_3 & -\dfrac{\partial \overline{V_1}}{\partial x_3}+C_s\zeta_2 \\ -\dfrac{\partial \overline{V_2}}{\partial x_1}+C_s\zeta_3 & -\dfrac{\partial \overline{V_2}}{\partial x_2} & -\dfrac{\partial \overline{V_2}}{\partial x_3}-C_s\zeta_1 \\ -\dfrac{\partial \overline{V_3}}{\partial x_1}-C_s\zeta_2 & -\dfrac{\partial \overline{V_3}}{\partial x_2}+C_s\zeta_1 & -\dfrac{\partial V_3}{\partial x_3} \end{vmatrix} \tag{5}$$

and $\vec{\zeta}=\mathrm{rot}\overline{\vec{V}}$.

In (3), the first term is the coefficient of friction due to the vortex motion of the flow, and the second takes into account the influence of the wall.

As can be seen from system (1), the first two equations are analogous to the system of Navier-Stokes equations averaged over Reynols. However, in the Reynolds equations, turbulent stresses are unknown. Consequently, the Reynolds equations are not closed, and for closing it is necessary to involve various hypotheses. As for the two-fluid approach, it gives a closed system of equations. Because for each unknown speed, an equation of motion is derived. The main difference between the two approaches is that they are based on different concepts. Reynolds' approach is based on the following hypotheses: 1) the turbulent flow velocity consists of the average and fluctuating velocities; 2) turbulent flow is described by the Navier-Stokes equation. It can be seen from these conditions that they are insufficient from the point of view of mathematics to describe turbulence. Because, based on the first hypothesis, two unknown speeds are introduced, and only one equation is used. Reynolds' first hypothesis can now be considered experimentally confirmed. As for the second, it has not yet been proven.

For the two-fluid approach, the main conditions are the first hypothesis of Reynolds and the fact that molar transfers of momentum and substances occur in a turbulent flow. In Ref. [44], based on the first Reynolds

hypothesis, the possibility of representing a turbulent flow as a heterogeneous mixture of two fluids was shown. These fluids do not fluctuate and fluctuations in velocity are due to the chaotic distribution of the volumes of these fluids. Those. the fluctuating parameter is the volume fraction of fluids in a given elementary volume and the time-averaged values of which are equal to 0.5. Therefore, writing the equations of motion for the first and second fluids, taking into account the interaction forces, after averaging over time, we obtain a system of turbulence equations in the two-fluid approach.

The system of equations of the two-fluid turbulence model (1) in Cartesian coordinates for the two-dimensional case can be written as:

$$\begin{cases} \dfrac{\partial U}{\partial t}+U\dfrac{\partial U}{\partial x}+V\dfrac{\partial U}{\partial y}+\dfrac{\partial p}{\rho\partial x}=\nu\left(\dfrac{\partial^2 U}{\partial y^2}+\dfrac{\partial^2 U}{\partial x^2}\right)-\dfrac{\partial \vartheta u}{\partial y}-\dfrac{\partial uu}{\partial x}, \\ \dfrac{\partial V}{\partial t}+U\dfrac{\partial V}{\partial x}+V\dfrac{\partial V}{\partial y}+\dfrac{\partial p}{\rho\partial y}=\nu\left(\dfrac{\partial^2 V}{\partial y^2}+\dfrac{\partial^2 V}{\partial x^2}\right)-\dfrac{\partial \vartheta\vartheta}{\partial y}-\dfrac{\partial u\vartheta}{\partial x}, \\ \dfrac{\partial u}{\partial t}+U\dfrac{\partial u}{\partial x}+V\dfrac{\partial u}{\partial y}=-\dfrac{\partial U}{\partial x}u-\dfrac{\partial U}{\partial y}\vartheta+C_s(\dfrac{\partial U}{\partial y}-\dfrac{\partial V}{\partial x})\vartheta+\dfrac{\partial}{\partial x}\left(2\nu_{xx}\dfrac{\partial u}{\partial x}\right)+\dfrac{\partial}{\partial y}\left(\nu_{xy}\left(\dfrac{\partial u}{\partial y}+\dfrac{\partial \vartheta}{\partial x}\right)\right)-K_f u, \\ \dfrac{\partial \vartheta}{\partial t}+U\dfrac{\partial \vartheta}{\partial x}+V\dfrac{\partial \vartheta}{\partial y}=-\dfrac{\partial V}{\partial y}\vartheta-\dfrac{\partial V}{\partial x}u-C_s(\dfrac{\partial U}{\partial y}-\dfrac{\partial V}{\partial x})u+\dfrac{\partial}{\partial x}\left(\nu_{xy}\left(\dfrac{\partial \vartheta}{\partial x}+\dfrac{\partial u}{\partial y}\right)\right)+\dfrac{\partial}{\partial y}\left(2\nu_{yy}\dfrac{\partial \vartheta}{\partial y}\right)-K_f\vartheta, \\ \dfrac{\partial U}{\partial x}+\dfrac{\partial V}{\partial y}=0, \end{cases} \tag{6}$$

Here

$$\nu_{xx}=\nu_{yy}=3\nu+2\frac{S}{\mathbf{defV}},\quad \nu_{xy}=3\nu+2\left|\frac{u,\vartheta}{\mathbf{defV}}\right|,\quad \mathbf{defV}=\sqrt{\left(\frac{\partial U}{\partial y}+\frac{\partial V}{\partial x}\right)^2+2\left(\frac{\partial U}{\partial x}\right)^2+2\left(\frac{\partial V}{\partial y}\right)^2}, \tag{7}$$

$$S=\frac{u^2J_x+\vartheta^2J_y}{J_x+J_y},\quad J_x=\left|\frac{\partial u}{\partial x}\right|,\quad J_y=\left|\frac{\partial \vartheta}{\partial y}\right|,\quad C_s=0.2,\quad K_f=C_1\lambda_{\max}+C_2\frac{|\mathbf{d}\cdot\mathbf{v}|}{d^2}.$$

In the above equations, U,V are, respectively, the longitudinal and transverse components of the averaged flow velocity vector, u, ϑ are similar relative velocities, $\nu_{xx},\nu_{yy},\nu_{xy}$ are effective molar viscosities, d is the nearest distance to a solid wall.

To determine the coefficient of friction, we make the characteristic equation (6):

$$\begin{vmatrix} -\lambda-\dfrac{\partial U}{\partial x} & -\dfrac{\partial U}{\partial y}+C_s(\dfrac{\partial U}{\partial y}-\dfrac{\partial V}{\partial x}) \\ -\dfrac{\partial V}{\partial x}-C_s(\dfrac{\partial U}{\partial y}-\dfrac{\partial V}{\partial x}) & -\lambda-\dfrac{\partial V}{\partial y} \end{vmatrix}=0. \tag{8}$$

From equation (8) we find the largest real root:

$$\begin{aligned} &\lambda_{\max}=\sqrt{D} \qquad \text{if} \quad D>0 \\ &\lambda_{\max}=0 \qquad \text{if} \quad D<0 \\ &D=\frac{\partial U}{\partial y}\frac{\partial V}{\partial x}-\frac{\partial U}{\partial x}\frac{\partial V}{\partial y}+C_s(1-C_s)\left[\frac{\partial U}{\partial y}-\frac{\partial V}{\partial x}\right]^2 \end{aligned} \tag{9}$$

4. Calculated grids

It is known that large velocity gradients occur in the mixing layers and near solid walls. In the problem under consideration, the processes occurring in the mixing layer of two streams are of great importance [50]. Therefore, in this study, a condensed computational grid was used, which is shown in Fig. 2. For the numerical implementation of the task, the computational domain is divided into three sections (Fig. 2).

As can be seen from Fig. 2, the grid was condensed in the central part of sections A, B, C and also in the section x = 0. To do this, the transformation of coordinate systems is used $(x,y)\rightarrow(\xi,\eta)$.

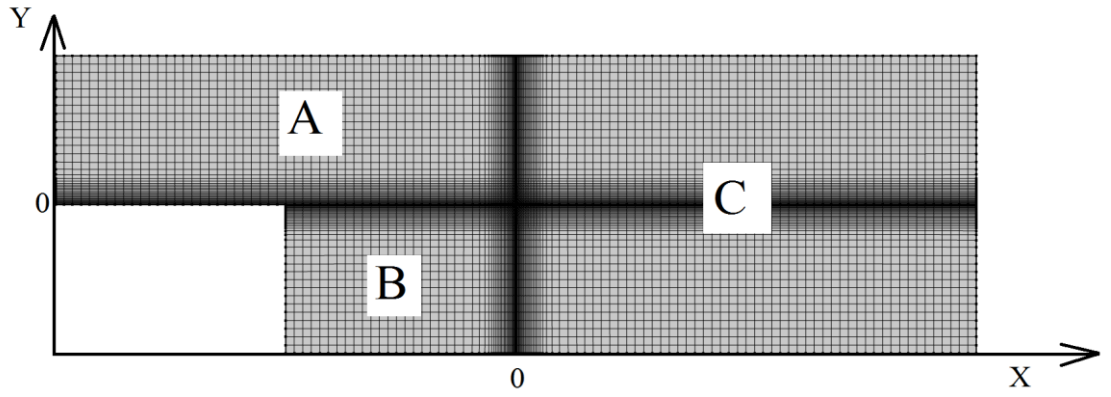

Figure. 2. Condensed grid

In the central section A, B, C, the following Y-coordinate transformation was used

$$\eta = y_c \left\{ 1 + \frac{\mathrm{sh}\left[\tau\left(y - B\right)\right]}{\mathrm{sh}\left(\tau B\right)} \right\}, \tag{10}$$

Here

$$B = \frac{1}{2\tau} \ln\left[\frac{1 + \left(e^{\tau} - 1\right)\left(y_c / h\right)}{1 + \left(e^{-\tau} - 1\right)\left(y_c / h\right)} \right], \; 0 < \tau < \infty. \tag{11}$$

τ- a stretching parameter that varies from zero to large values.

In sections A and B, at x=0, the X coordinate transformation is used.

$$\xi = \alpha + \left(1 - \alpha\right) \frac{\ln\left(\left\{ \beta + \left[x\left(2\alpha + 1\right) / \mathrm{L} \right] - 2\alpha \right\} / \left\{ \beta - \left[x\left(2\alpha + 1\right) / \mathrm{L} \right] + 2\alpha \right\} \right)}{\ln\left[\left(\beta + 1\right) / \left(\beta - 1\right) \right]}. \tag{12}$$

This transformation at $\alpha = 0$ allows you to grind the calculated grid in the section $x = 0$. The β parameter is about 1 and regulates the degree of grinding. The work uses the value $\beta = 1.054.$

In section C, the X-coordinate transformation is used in the section $x = 0$.

$$\xi = 1 - \frac{\ln\left(\left\{ \beta + 1 - x / \mathrm{M} \right\} / \left\{ \beta - 1 + x / M \right\} \right)}{\ln\left[\left(\beta + 1\right) / \left(\beta - 1\right) \right]}, \quad 1 < \beta < \infty. \tag{13}$$

The value is also used here $\beta = 1.054.$ The number of grids of calculation nodes on site A is 100×80, on site B is 50×80 and on site C is 200×164.

The system of equations (6) after the transformation of coordinates in dimensionless parameters has the form:

$$\begin{cases}
\dfrac{\partial U}{\partial t} + U\dfrac{\partial \xi}{\partial x}\dfrac{\partial U}{\partial \xi} + V\dfrac{\partial \eta}{\partial y}\dfrac{\partial U}{\partial \eta} + \dfrac{\partial \xi}{\rho \partial x}\dfrac{\partial p}{\partial \xi} = \dfrac{1}{\mathrm{Re}}\left(\left(\dfrac{\partial \xi}{\partial x}\right)^2 \dfrac{\partial U}{\partial \xi^2} + \left(\dfrac{\partial \eta}{\partial y}\right)^2 \dfrac{\partial^2 U}{\partial \eta^2} \right) - \dfrac{\partial \xi}{\partial x}\dfrac{\partial uu}{\partial \xi} - \dfrac{\partial \eta}{\partial y}\dfrac{\partial u\vartheta}{\partial \eta}; \\
\dfrac{\partial V}{\partial t} + U\dfrac{\partial \xi}{\partial x}\dfrac{\partial V}{\partial \xi} + V\dfrac{\partial \eta}{\partial y}\dfrac{\partial V}{\partial \eta} + \dfrac{\partial \eta}{\rho \partial y}\dfrac{\partial p}{\partial \eta} = \dfrac{1}{\mathrm{Re}}\left(\left(\dfrac{\partial \xi}{\partial x}\right)^2 \dfrac{\partial V}{\partial \xi^2} + \left(\dfrac{\partial \eta}{\partial y}\right)^2 \dfrac{\partial^2 V}{\partial \eta^2} \right) - \dfrac{\partial \xi}{\partial x}\dfrac{\partial u\vartheta}{\partial \xi} - \dfrac{\partial \eta}{\partial y}\dfrac{\partial \vartheta\vartheta}{\partial \eta}; \\
\dfrac{\partial u}{\partial t} + U\dfrac{\partial \xi}{\partial x}\dfrac{\partial u}{\partial \xi} + V\dfrac{\partial \eta}{\partial y}\dfrac{\partial u}{\partial \eta} = -\left(u\dfrac{\partial \xi}{\partial x}\dfrac{\partial U}{\partial \xi} + \vartheta\dfrac{\partial \eta}{\partial y}\dfrac{\partial U}{\partial \eta} \right) + C_s\left(-\left(\dfrac{\partial \xi}{\partial x}\dfrac{\partial V}{\partial \xi} - \dfrac{\partial \eta}{\partial y}\dfrac{\partial U}{\partial \eta} \right)\vartheta \right) + \\
\qquad + \dfrac{\partial \xi}{\partial x}\dfrac{\partial}{\partial \xi}\left(2\nu_{xx}\left(\dfrac{\partial \xi}{\partial x}\dfrac{\partial u}{\partial \xi} \right) \right) + \dfrac{\partial \eta}{\partial y}\dfrac{\partial}{\partial \eta}\left(\nu_{xy}\left(\dfrac{\partial \eta}{\partial y}\dfrac{\partial u}{\partial \eta} + \dfrac{\partial \xi}{\partial x}\dfrac{\partial \vartheta}{\partial \xi} \right) \right) - K_f u; \\
\dfrac{\partial \vartheta}{\partial t} + U\dfrac{\partial \xi}{\partial x}\dfrac{\partial \vartheta}{\partial \xi} + V\dfrac{\partial \eta}{\partial y}\dfrac{\partial \vartheta}{\partial \eta} = -\left(u\dfrac{\partial \xi}{\partial x}\dfrac{\partial \vartheta}{\partial \xi} + \vartheta\dfrac{\partial \eta}{\partial y}\dfrac{\partial V}{\partial \eta} \right) + C_s\left(\left(\dfrac{\partial \xi}{\partial x}\dfrac{\partial V}{\partial \xi} - \dfrac{\partial \eta}{\partial y}\dfrac{\partial U}{\partial \eta} \right)u \right) + \\
\qquad + \dfrac{\partial \xi}{\partial x}\dfrac{\partial}{\partial \xi}\left(\nu_{xy}\left(\dfrac{\partial \xi}{\partial x}\dfrac{\partial \vartheta}{\partial \xi} + \dfrac{\partial \eta}{\partial y}\dfrac{\partial u}{\partial \eta} \right) \right) + \dfrac{\partial \eta}{\partial y}\dfrac{\partial}{\partial \eta}\left(2\nu_{yy}\dfrac{\partial \eta}{\partial y}\dfrac{\partial \vartheta}{\partial \eta} \right) - K_f \vartheta; \\
\dfrac{\partial \xi}{\partial x}\dfrac{\partial U}{\partial \xi} + \dfrac{\partial \eta}{\partial y}\dfrac{\partial V}{\partial \eta} = 0.
\end{cases} \tag{14}$$

Here

$$\nu_{xx}=\nu_{yy}=\frac{3}{\mathrm{Re}}+2\frac{S}{|\mathbf{defV}|},\ \ \nu_{xy}=\frac{3}{\mathrm{Re}}+2\left|\frac{u\vartheta}{\mathbf{defV}}\right|,\ S=\frac{u^2J_x+\vartheta^2J_y}{J_x+J_y},\ J_x=\left|\frac{\partial\xi}{\partial x}\frac{\partial u}{\partial\xi}\right|,\ J_y=\left|\frac{\partial\eta}{\partial y}\frac{\partial\vartheta}{\partial\eta}\right|,$$
$$|\mathbf{defV}|=\sqrt{2\left(\left(\frac{\partial\xi}{\partial x}\frac{\partial U}{\partial\xi}\right)^2+\left(\frac{\partial\eta}{\partial y}\frac{\partial V}{\partial\eta}\right)^2\right)+\left(\frac{\partial\xi}{\partial x}\frac{\partial V}{\partial\xi}+\frac{\partial\eta}{\partial y}\frac{\partial U}{\partial\eta}\right)^2}\ C_s=0.2,\ \ K_f=C_1\lambda_{\max}+C_2\frac{|\mathbf{d}\cdot\mathbf{v}|}{d^2} \tag{15}$$

The system of equations (6, 14) can be represented in matrix form:

$$\frac{\partial\Phi}{\partial t}+U\frac{\partial\Phi}{\partial x}+V\frac{\partial\Phi}{\partial y}=\frac{\partial}{\partial x}\left(\mathrm{A}\frac{\partial\Phi}{\partial x}\right)+\frac{\partial}{\partial y}\left(\mathrm{B}\frac{\partial\Phi}{\partial y}\right)+\Pi^{\Phi}. \tag{16}$$

Here

$$\Phi=\begin{pmatrix}U\\V\\u\\\vartheta\end{pmatrix},\ \mathrm{A}=\begin{pmatrix}\frac{1}{\mathrm{Re}}\\\frac{1}{\mathrm{Re}}\\2\nu_{xx}\\\nu_{xy}\end{pmatrix},\ \mathrm{B}=\begin{pmatrix}\frac{1}{\mathrm{Re}}\\\frac{1}{\mathrm{Re}}\\\nu_{xy}\\2\nu_{yy}\end{pmatrix},\ \Pi^{\Phi}=\begin{pmatrix}-\frac{\partial p}{\rho\partial x}-\frac{\partial\vartheta u}{\partial y}-\frac{\partial uu}{\partial x}\\-\frac{\partial p}{\rho\partial y}-\frac{\partial\vartheta\vartheta}{\partial y}-\frac{\partial u\vartheta}{\partial x}\\-\left(u\frac{\partial U}{\partial x}+\vartheta\frac{\partial U}{\partial y}\right)+\frac{\partial}{\partial y}\left(\nu_{xy}\left(\frac{\partial\vartheta}{\partial x}\right)\right)+C_s\left(-\left(\frac{\partial V}{\partial x}-\frac{\partial U}{\partial y}\right)\vartheta\right)-K_fu\\-\left(u\frac{\partial V}{\partial x}+\vartheta\frac{\partial V}{\partial y}\right)+\frac{\partial}{\partial x}\left(\nu_{xy}\left(\frac{\partial u}{\partial y}\right)\right)+C_s\left(\left(\frac{\partial V}{\partial x}-\frac{\partial U}{\partial y}\right)u\right)-K_f\vartheta\end{pmatrix}.$$

The system of equations (14) was reduced to a dimensionless form by correlating all velocities to the average velocity at the inlet of the upper stream, and spatial dimensions to the height of the channel. The Reynolds number was $\mathrm{Re}_H=415400$. At the entrance to the computational domain, an experimental velocity profile was set, as well as initial dimensionless perturbations of relative velocities $u=0.02,\ \vartheta=0.$ Adhesion conditions were set on the walls. At the output x=1200 mm, extrapolation conditions of the second order of accuracy were set [10].

5. Numerical schemes

5.1. Explicit Upwind Scheme-(EUS)

In computational physics, anti-flow schemes denote a class of numerical discretization method for solving hyperbolic partial differential equations. Anti-flow schemes use an adaptive or solution-sensitive finite difference pattern to numerically simulate the direction of information propagation in the flow field. In the schemes against the flow, an attempt is made to discredit partial differential equations of hyperbolic type using a difference shifted in the direction determined by the sign of the characteristic velocities against the flow. This method is especially convenient for solving nonlinear partial differential equations, such as the Euler and Navier-Stokes equations. An explicit scheme against the flow can be represented as:

$$\frac{\Phi_{i,j}^{n+1}-\Phi_{i,j}^{n}}{\Delta t}+\frac{\left(F_e+|F_e|\right)\Phi_{i+1,j}^{n}+\left(|F_e|+|F_w|+F_e-F_w\right)\Phi_{i,j}^{n}-\left(F_w+|F_w|\right)\Phi_{i-1,j}^{n}}{2\Delta x}+$$
$$+\frac{\Phi_{i,j+1}^{n}\left(F_n-|F_n|\right)+\Phi_{i,j}^{n}\left(\left(|F_n|+F_n\right)+\left(|F_s|-F_s\right)\right)-\Phi_{i,j-1}^{n}\left(|F_s|+F_s\right)}{2\Delta y}= \tag{17}$$
$$=\frac{1}{\mathrm{Re}}\left(\frac{\Phi_{i+1,j}^{n}-2\Phi_{i,j}^{n}+\Phi_{i-1,j}^{n}}{\Delta x^2}+\frac{\Phi_{i,j+1}^{n}-2\Phi_{i,j}^{n}+\Phi_{i,j-1}^{n}}{\Delta y^2}\right)-\Pi^{\Phi}$$

Here

$$F_e=\frac{\left(U_{i+1,j}^{n}+U_{i,j}^{n}\right)}{2},\ \ F_w=\frac{\left(U_{i,j}^{n}+U_{i-1,j}^{n}\right)}{2},$$
$$F_n=\frac{\left(V_{i,j+1}^{n}+V_{i,j}^{n}\right)}{2},\ \ F_s=\frac{\left(V_{i,j}^{n}+V_{i,j-1}^{n}\right)}{2}.$$

This scheme has first-order accuracy in time and space. Therefore, the approximation error is equal to $O\left((\Delta t),(\Delta x),(\Delta y)\right)$. The stability condition is $\left(\frac{U_{\max}\Delta t}{\Delta x}+\frac{V_{\max}\Delta t}{\Delta y}\right)\le 1$.

Integration was carried out in time steps $\Delta t<0.0005$.

5.2. Semi-Implicit Upwind Scheme-(SIUS)

The paper uses a semi-implicit scheme against the flow, which is a two-step scheme and is similar to the Peaceman-Rachford scheme. In this scheme, all convective terms in the hydrodynamic equations were approximated against the flow as in the explicit scheme, and diffusion terms in a semi-implicit form as in the Peaceman-Rachford scheme [51]:

Step 1

$$\frac{\overline{\Phi}_{i,j}^{n+1}-\Phi_{i,j}^{n}}{\Delta t}+\frac{\left(F_e+|F_e|\right)\overline{\Phi}_{i+1,j}^{n+1}+\left(|F_e|+|F_w|+F_e-F_w\right)\overline{\Phi}_{i,j}^{n+1}-\left(F_w+|F_w|\right)\overline{\Phi}_{i-1,j}^{n+1}}{2\Delta x}+$$
$$+\frac{\Phi_{i,j+1}^{n}\left(F_n-|F_n|\right)+\Phi_{i,j}^{n}\left(\left(|F_n|+F_n\right)+\left(|F_s|-F_s\right)\right)-\Phi_{i,j-1}^{n}\left(|F_s|+F_s\right)}{2\Delta y}= \tag{18}$$
$$=\frac{1}{\mathrm{Re}}\left(\frac{\overline{\Phi}_{i+1,j}^{n+1}-2\overline{\Phi}_{i,j}^{n+1}+\overline{\Phi}_{i-1,j}^{n+1}}{\Delta x^2}+\frac{\Phi_{i,j+1}^{n}-2\Phi_{i,j}^{n}+\Phi_{i,j-1}^{n}}{\Delta y^2}\right)-\Pi^{\Phi}$$

Here

$$F_e=\frac{\left(U_{i+1,j}^{n}+U_{i,j}^{n}\right)}{2},\quad F_w=\frac{\left(U_{i,j}^{n}+U_{i-1,j}^{n}\right)}{2},$$
$$F_n=\frac{\left(V_{i,j+1}^{n}+V_{i,j}^{n}\right)}{2},\quad F_s=\frac{\left(V_{i,j}^{n}+V_{i,j-1}^{n}\right)}{2}.$$

Step 2

$$\frac{\Phi_{i,j}^{n+1}-\overline{\Phi}_{i,j}^{n+1}}{\Delta t}+\frac{\left(F_e+|F_e|\right)\overline{\Phi}_{i+1,j}^{n+1}+\left(|F_e|+|F_w|+F_e-F_w\right)\overline{\Phi}_{i,j}^{n+1}-\left(F_w+|F_w|\right)\overline{\Phi}_{i-1,j}^{n+1}}{2\Delta x}+$$
$$+\frac{\Phi_{i,j+1}^{n+1}\left(F_n-|F_n|\right)+\Phi_{i,j}^{n+1}\left(\left(|F_n|+F_n\right)+\left(|F_s|-F_s\right)\right)-\Phi_{i,j-1}^{n+1}\left(|F_s|+F_s\right)}{2\Delta y}= \tag{19}$$
$$=\frac{1}{\mathrm{Re}}\left(\frac{\overline{\Phi}_{i+1,j}^{n+1}-2\overline{\Phi}_{i,j}^{n+1}+\overline{\Phi}_{i-1,j}^{n+1}}{\Delta x^2}+\frac{\Phi_{i,j+1}^{n+1}-2\Phi_{i,j}^{n+1}+\Phi_{i,j-1}^{n+1}}{\Delta y^2}\right)-\Pi^{\Phi}$$

Here

$$F_e=\frac{\left(\overline{U}_{i+1,j}^{n}+\overline{U}_{i,j}^{n}\right)}{2},\quad F_w=\frac{\left(\overline{U}_{i,j}^{n}+\overline{U}_{i-1,j}^{n}\right)}{2},$$
$$F_n=\frac{\left(\overline{V}_{i,j+1}^{n}+\overline{V}_{i,j}^{n}\right)}{2},\quad F_s=\frac{\left(\overline{V}_{i,j}^{n}+\overline{V}_{i,j-1}^{n}\right)}{2}.$$

The scheme used has an approximation error of $O((\Delta t),(\Delta x),(\Delta y))$ To determine the unknown $\Phi_{i+1,j}^{n+1},\Phi_{i-1,j}^{n+1},\Phi_{i,j+1}^{n+1},\Phi_{i,j-1}^{n+1}$, a sweep method was used. The integration was carried out in time steps $\Delta t<0.05$.

6. Solution method

The finite volume method is used for the numerical solution of the system of initial nonstationary equations (14). For the numerical realization of the equations, a staggered calculation scheme is used, where the velocity and pressure components are determined at various nodes. The SIMPLE method was used to correct averaged velocities through pressures [52].

7. Results of numerical experiments and their discussion

Figure 3 shows graphs in different channel sections for dimensionless longitudinal velocity based on the results of a two-fluid turbulence model using various numerical schemes. Experimental data are also provided for comparison. The figures show the profiles of the axial U-component of the velocity in different sections of the channel. Here U1=22.40 m/s, ΔU=19.14 m/s and δw=13.771 mm at x=200 mm, δw=35.894 mm at x=650 mm, δw=50.547 mm at x=950mm.

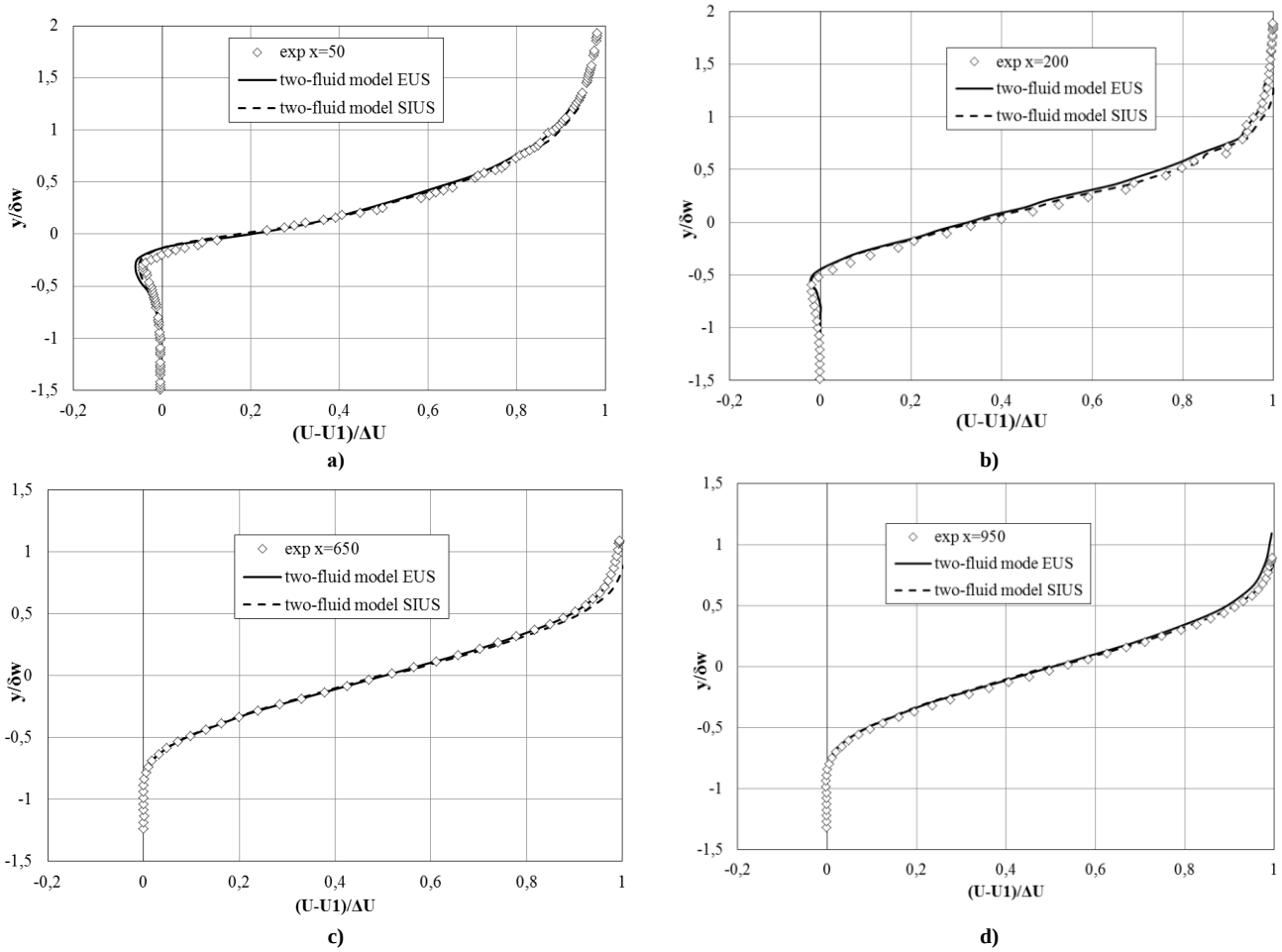

Figure. 3. Profiles of dimensionless axial velocity at different channel sections

Figure 4 shows the profiles of turbulent stress in various cross sections.

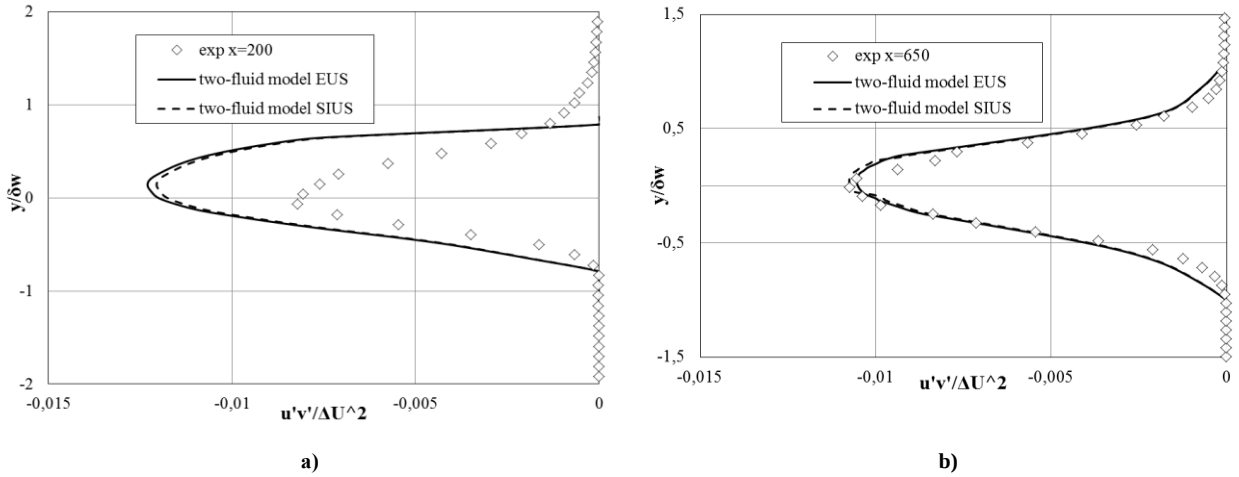

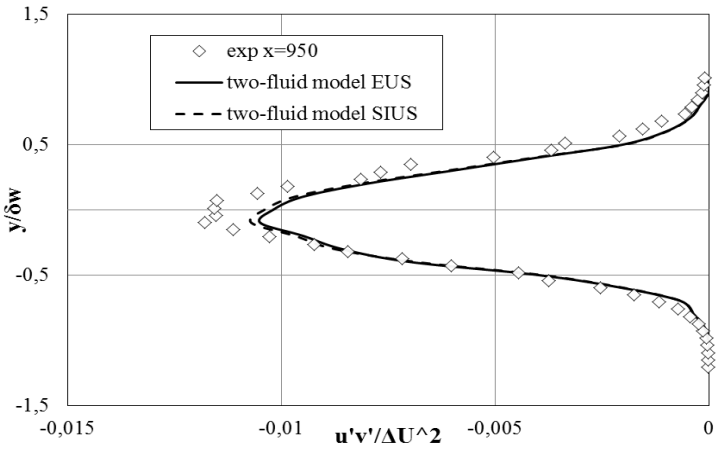

c)

Figure. 4. Profiles of turbulent stress at different cross-sections of channels

Table 1 shows the results of the axial speed for various sections of the channels

x = 50 mm				x = 200 mm				x = 650 mm			
y/δw	**Exp**	**EUS**	**SIUS**	**y/δw**	**Exp**	**EUS**	**SIUS**	**y/δw**	**exp**	**EUS**	**SIUS**
-1.24	-0.00418	-0.0041	-0.00349	**-1.08**	-0.00327	0	0	**-1.23898**	0.000152	0.000152	0.000149
-1.12	-0.00477	-0.0039	-0.00332	**-0.94**	-0.00679	0	0	**-1.20137**	0.000188	0.000188	0.000184
-1.01	-0.00446	-0.0044	-0.00374	**-0.87**	-0.01102	0	0	**-1.15122**	0.000596	0.000596	0.000584
-0.9	-0.0064	-0.0053	-0.00451	**-0.79**	-0.01396	0	0	**-1.13869**	0.000507	0.000507	0.000497
-0.79	-0.00896	-0.01	-0.0085	**-0.65**	-0.01919	-0.01	-0.009	**-1.12615**	0.000564	0.000564	0.000553
-0.67	-0.01364	-0.02	-0.017	**-0.58**	-0.01918	-0.022	-0.0198	**-1.11361**	0.000486	0.000486	0.000476
-0.56	-0.0209	-0.03	-0.0255	**-0.5**	0.004269	-0.017	-0.0153	**-1.10108**	0.004269	0.000334	0.000328
-0.45	-0.0294	-0.05	-0.0425	**-0.43**	0.030308	0.0063	0.006615	**-1.05093**	0.000334	-3.1E-05	-3.1E-05
-0.33	-0.04285	-0.06	-0.051	**-0.36**	0.072952	0.042	0.0441	**-1.00078**	-0.00031	-0.00031	-0.0003
-0.22	-0.01157	-0.05	-0.0425	**-0.29**	0.12802	0.083	0.08715	**-0.90048**	2.09E-05	2.09E-05	2.05E-05
-0.112	0.081547	0.02	0.017	**-0.21**	0.168856	0.15	0.1575	**-0.80019**	0.004451	0.004451	0.004362
0	0.124718	0.2	0.17	**-0.14**	0.240569	0.2151	0.225855	**-0.69989**	0.015261	0.015261	0.014956
0.112	0.322999	0.3423	0.349146	**-0.07**	0.322602	0.2643	0.277515	**-0.5996**	0.044201	0.044201	0.043317
0.22	0.484295	0.44	0.4488	**0**	0.365684	0.3258	0.34209	**-0.51184**	0.083783	0.083783	0.082107
0.33	0.564305	0.53	0.5406	**0.07**	0.441907	0.38	0.399	**-0.43662**	0.130428	0.130428	0.12782
0.45	0.655073	0.62	0.6324	**0.14**	0.510731	0.45	0.4725	**-0.31125**	0.217879	0.217879	0.213521
0.56	0.712142	0.7	0.714	**0.21**	0.569431	0.5	0.525	**-0.22349**	0.295538	0.295538	0.289627
0.67	0.773725	0.76	0.7752	**0.29**	0.660308	0.58	0.609	**-0.11066**	0.400805	0.400805	0.392788
0.79	0.818333	0.811	0.82722	**0.36**	0.683532	0.65	0.6825	**-0.09812**	0.412492	0.412492	0.404242
0.9	0.861933	0.8567	0.873834	**0.43**	0.748025	0.7	0.735	**-0.08559**	0.42442	0.42442	0.415932
1.02	0.89001	0.8852	0.902904	**0.5**	0.785037	0.75	0.7875	**-0.03544**	0.470831	0.470831	0.461414
1.12	0.910355	0.9053	0.923406	**0.58**	0.824922	0.8	0.84	**-0.0229**	0.482388	0.482388	0.47274
1.24	0.9321	0.9261	0.944622	**0.65**	0.895387	0.8362	0.852924	**-0.01036**	0.494065	0.494065	0.484183
				0.79	0.932189	0.9212	0.939624	**0.002173**	0.506625	0.506625	0.496492
				0.87	0.945188	0.9359	0.954618	**0.039784**	0.541693	0.541693	0.552527
				0.94	0.938767	0.9474	0.966348	**0.052321**	0.55348	0.55348	0.564549

1.08	0.96245	0.97	0.9894	**0.089931**	0.586771	0.586771	0.598506
1.23	0.983584	0.98	0.9996	**0.102468**	0.599206	0.599206	0.61119
1.3	0.988041	0.98	0.9996	**0.115005**	0.610454	0.610454	0.622664
1.37	0.989572	0.99	1.0098	**0.127542**	0.622377	0.622377	0.634825
1.45	0.991113	0.99	1.0098	**0.140079**	0.634007	0.634007	0.646687
				0.152616	0.645334	0.645334	0.658241
				0.165153	0.656766	0.656766	0.669901
				0.202764	0.690329	0.690329	0.704136
				0.303059	0.769159	0.769159	0.784542
				0.415891	0.847942	0.847942	0.8649
				0.50365	0.895914	0.895914	0.913832
				0.616482	0.9386	0.9386	0.957372
				0.70424	0.961045	0.961045	0.980266
				0.829609	0.977576	0.977576	0.997127
				0.917368	0.985068	0.985068	1.004769
				1.017663	0.990026	0.990026	1.009827
				1.042737	0.99151	0.99151	1.01134
				1.067811	0.992163	0.992826	1.012683

As can be seen from Fig. 4, at close distances, the numerical results differ quite significantly from the experimental ones. Therefore, the results of the well-known Spalart-Allmaras SA [40], Menter SST [41] and Reynolds stress models SSG LRR-RSM [47] were also obtained to check the reliability. On fig. Figures 5-6 show the results of the axial velocity profiles and turbulent stress profiles in different sections of the channel.

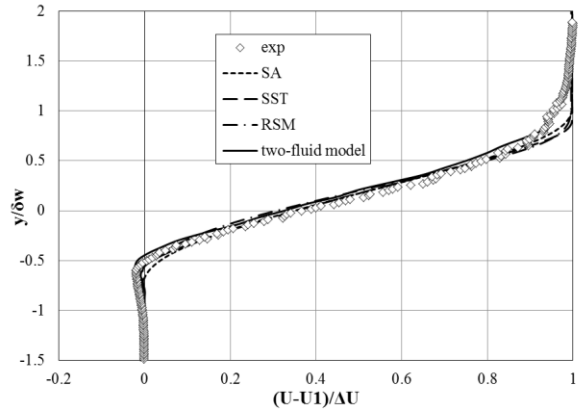

a)

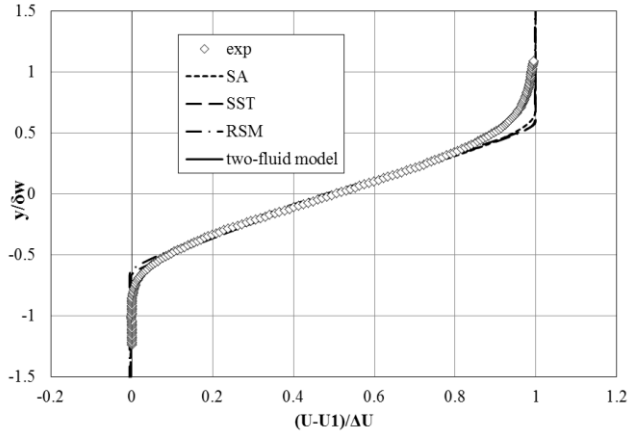

b)

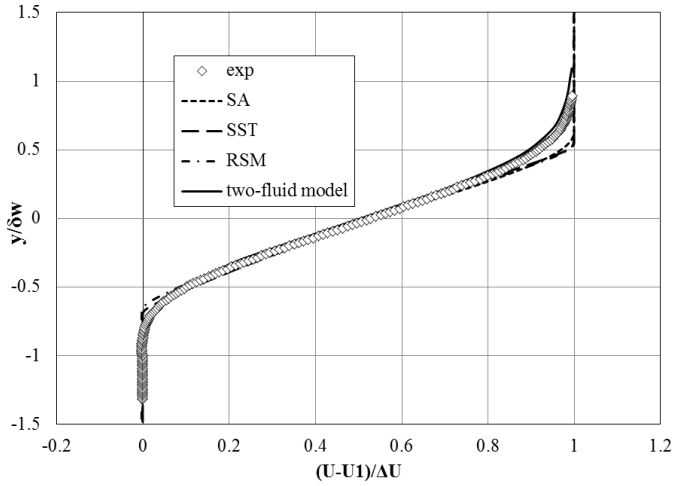

c)

Figure. 5. Axial velocity profiles for various channel sections x = 200 mm, b) at x = 650 mm, c) at x = 950 mm

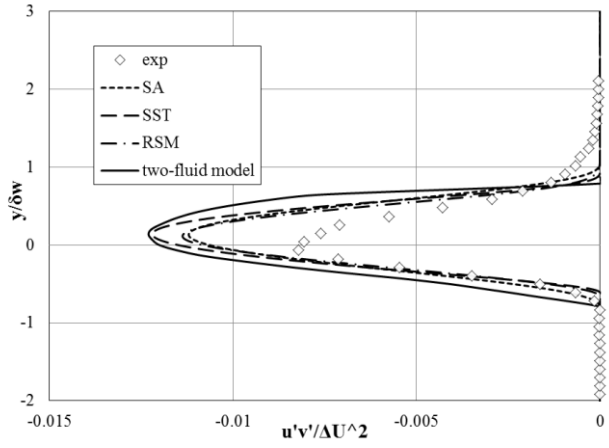

a)

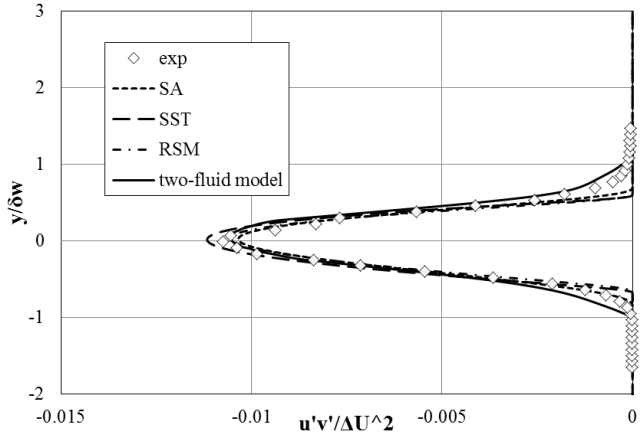

b)

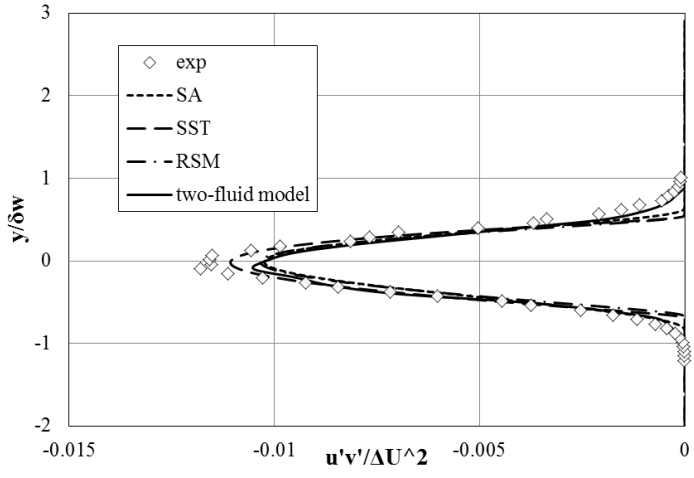

c)

Figure. 6. Profiles of turbulent stress for different sections of channels x = 200 mm, b) at x = 650 mm, c) at x = 950 mm

It can be seen from the figures that the results of all models, despite the different approaches, are in good agreement with each other. Good agreement with the experimental data is observed for the longitudinal velocity profiles for various channel sections. As for turbulent stresses, good agreement with experimental data occurs far from the plate and, for unknown reasons, somewhat worse near it. From the presented figures, one can also judge that the results are practically independent of difference schemes for numerical implementation. However, the semi-implicit scheme makes it possible to carry out numerical calculations with much larger time steps than when using the explicit scheme.

8. Conclusion

- The paper presents the numerical results of mixing two incompressible viscous fluids in a flat channel using the well-known Spalart-Allmaras SA, Menter SST and Reynolds stresses SSG LRR-RSM models, as well as a two-fluid turbulent model. Velocity and turbulent stress profiles are demonstrated for various channel sections. Numerical implementation of the models showed that all of them practically give the same results. However, the computational costs for numerical implementation for each model turned out to be different. The models of Menter SST and Reynolds stresses SSG LRR-RSM turned out to be very demanding on the computational grid, as well as on the integration time. These models require a high resolution of computational grids and, for stability, it is necessary to integrate with sufficiently small-time steps. The two-fluid model turned out to be the least demanding on computing resources. This model retained its stability even with a 20-fold increase in the time step than was required to implement the Spalart-Allmaras SA model. It should be noted that the results of the two-fluid model turned out to be practically independent of the choice of difference schemes. The obtained results showed that the two-fluid model has a fairly good accuracy, is easy to implement numerically, and has a high stability. Therefore, it can be recommended for calculations of more complex turbulent flows.

References

[1] M. R. Gorji, S. Cosyns, C. Debbaut, G. Ghorbaniasl, W. Willaert, W. Ceelen, Analysis of the effect of liquid viscosity on the aerosol distribution during Pressurized Intraperitoneal Aerosol Chemotherapy (PIPAC) using computational modeling, *European Journal of Surgical Oncology*, Vol. 48, No. 2, pp. e159, 2022.

[2] M. R. Gorji, C. Debbaut, G. Ghorbaniasl, W. Willaert, S. Cosyns, W. Ceelen, Electrostatic precipitation pressurized intraperitoneal aerosol chemotherapy (ePIPAC): Finding the optimal electrical potential, *European Journal of Surgical Oncology*, Vol. 47, No. 2, pp. e30, 2021.

[3] M. Rahimi-Gorji, G. Ghorbaniasl, S. Cosyns, W. Willaert, W. Ceelen, Effect of fluid flow rate and droplet size on spatial aerosol distribution during pressurized intraperiational aerosol chemotherapy (PIPAC), in *Proceeding of*.

[4] H. Asemi, S. Asemi, A. Farajpour, M. Mohammadi, Nanoscale mass detection based on vibrating piezoelectric ultrathin films under thermo-electro-mechanical loads, *Physica E: Low-dimensional Systems and Nanostructures*, Vol. 68, pp. 112-122, 2015.

[5] S. Asemi, A. Farajpour, H. Asemi, M. Mohammadi, Influence of initial stress on the vibration of double-piezoelectric-nanoplate systems with various boundary conditions using DQM, *Physica E: Low-dimensional Systems and Nanostructures*, Vol. 63, pp. 169-179, 2014.

[6] S. Asemi, A. Farajpour, M. Mohammadi, Nonlinear vibration analysis of piezoelectric nanoelectromechanical resonators based on nonlocal elasticity theory, *Composite Structures*, Vol. 116, pp. 703-712, 2014.

[7] S. R. Asemi, M. Mohammadi, A. Farajpour, A study on the nonlinear stability of orthotropic single-layered graphene sheet based on nonlocal elasticity theory, *Latin American Journal of Solids and Structures*, Vol. 11, No. 9, pp. 1515-1540, 2014.

[8] M. Baghani, M. Mohammadi, A. Farajpour, Dynamic and stability analysis of the rotating nanobeam in a nonuniform magnetic field considering the surface energy, *International Journal of Applied Mechanics*, Vol. 8, No. 04, pp. 1650048, 2016.

[9] !!! INVALID CITATION !!! [4-35].

[10] A. Farajpour, M. Mohammadi, A. Shahidi, M. Mahzoon, Axisymmetric buckling of the circular graphene sheets with the nonlocal continuum plate model, *Physica E: Low-dimensional Systems and Nanostructures*, Vol. 43, No. 10, pp. 1820-1825, 2011.

[11] M. Mohammadi, A. Rastgoo, Primary and secondary resonance analysis of FG/lipid nanoplate with considering porosity distribution based on a nonlinear elastic medium, *Mechanics of Advanced Materials and Structures*, Vol. 27, No. 20, pp. 1709-1730, 2020.

[12] M. Mohammadi, M. Hosseini, M. Shishesaz, A. Hadi, A. Rastgoo, Primary and secondary resonance analysis of porous functionally graded nanobeam resting on a nonlinear foundation subjected to mechanical and electrical loads, *European Journal of Mechanics-A/Solids*, Vol. 77, pp. 103793, 2019.

[13] M. Mohammadi, A. Rastgoo, Nonlinear vibration analysis of the viscoelastic composite nanoplate with three directionally imperfect porous FG core, *Structural Engineering and Mechanics, An Int'l Journal*, Vol. 69, No. 2, pp. 131-143, 2019.

[14] A. Farajpour, A. Rastgoo, M. Mohammadi, Vibration, buckling and smart control of microtubules using piezoelectric nanoshells under electric voltage in thermal environment, *Physica B: Condensed Matter*, Vol. 509, pp. 100-114, 2017.

[15] A. Farajpour, M. H. Yazdi, A. Rastgoo, M. Loghmani, M. Mohammadi, Nonlocal nonlinear plate model for large amplitude vibration of magneto-electro-elastic nanoplates, *Composite Structures*, Vol. 140, pp. 323-336, 2016.

[16] A. Farajpour, M. Yazdi, A. Rastgoo, M. Mohammadi, A higher-order nonlocal strain gradient plate model for buckling of orthotropic nanoplates in thermal environment, *Acta Mechanica*, Vol. 227, No. 7, pp. 1849-1867, 2016.

[17] M. R. Farajpour, A. Rastgoo, A. Farajpour, M. Mohammadi, Vibration of piezoelectric nanofilm-based electromechanical sensors via higher-order non-local strain gradient theory, *Micro & Nano Letters*, Vol. 11, No. 6, pp. 302-307, 2016.

[18] M. Mohammadi, M. Safarabadi, A. Rastgoo, A. Farajpour, Hygro-mechanical vibration analysis of a rotating viscoelastic nanobeam embedded in a visco-Pasternak elastic medium and in a nonlinear thermal environment, *Acta Mechanica*, Vol. 227, No. 8, pp. 2207-2232, 2016.

[19] M. Safarabadi, M. Mohammadi, A. Farajpour, M. Goodarzi, Effect of surface energy on the vibration analysis of rotating nanobeam, 2015.

[20] A. Farajpour, A. Rastgoo, M. Mohammadi, Surface effects on the mechanical characteristics of microtubule networks in living cells, *Mechanics Research Communications*, Vol. 57, pp. 18-26, 2014.

[21] M. Goodarzi, M. Mohammadi, A. Farajpour, M. Khooran, Investigation of the effect of pre-stressed on vibration frequency of rectangular nanoplate based on a visco-Pasternak foundation, 2014.

[22] M. Mohammadi, A. Farajpour, M. Goodarzi, F. Dinari, Thermo-mechanical vibration analysis of annular and circular graphene sheet embedded in an elastic medium, *Latin American Journal of Solids and Structures*, Vol. 11, pp. 659-682, 2014.

[23] M. Mohammadi, A. Farajpour, M. Goodarzi, Numerical study of the effect of shear in-plane load on the vibration analysis of graphene sheet embedded in an elastic medium, *Computational Materials Science*, Vol. 82, pp. 510-520, 2014.

[24] M. Mohammadi, A. Farajpour, A. Moradi, M. Ghayour, Shear buckling of orthotropic rectangular graphene sheet embedded in an elastic medium in thermal environment, *Composites Part B: Engineering*, Vol. 56, pp. 629-637, 2014.

[25] M. Mohammadi, A. Moradi, M. Ghayour, A. Farajpour, Exact solution for thermo-mechanical vibration of orthotropic mono-layer graphene sheet embedded in an elastic medium, *Latin American Journal of Solids and Structures*, Vol. 11, No. 3, pp. 437-458, 2014.

[26] M. Mohammadi, A. Farajpour, M. Goodarzi, R. Heydarshenas, Levy type solution for nonlocal thermo-mechanical vibration of orthotropic mono-layer graphene sheet embedded in an elastic medium, *Journal of Solid Mechanics*, Vol. 5, No. 2, pp. 116-132, 2013.

[27] M. Mohammadi, A. Farajpour, M. Goodarzi, H. Mohammadi, Temperature Effect on Vibration Analysis of Annular Graphene Sheet Embedded on Visco-Pasternak Foundati, *Journal of Solid Mechanics*, Vol. 5, No. 3, pp. 305-323, 2013.

[28] M. Mohammadi, M. Ghayour, A. Farajpour, Free transverse vibration analysis of circular and annular graphene sheets with various boundary conditions using the nonlocal continuum plate model, *Composites Part B: Engineering*, Vol. 45, No. 1, pp. 32-42, 2013.

[29] M. Mohammadi, M. Goodarzi, M. Ghayour, A. Farajpour, Influence of in-plane pre-load on the vibration frequency of circular graphene sheet via nonlocal continuum theory, *Composites Part B: Engineering*, Vol. 51, pp. 121-129, 2013.

[30] M. Danesh, A. Farajpour, M. Mohammadi, Axial vibration analysis of a tapered nanorod based on nonlocal elasticity theory and differential quadrature method, *Mechanics Research Communications*, Vol. 39, No. 1, pp. 23-27, 2012.

[31] A. Farajpour, A. Shahidi, M. Mohammadi, M. Mahzoon, Buckling of orthotropic micro/nanoscale plates under linearly varying in-plane load via nonlocal continuum mechanics, *Composite Structures*, Vol. 94, No. 5, pp. 1605-1615, 2012.

[32] M. Mohammadi, M. Goodarzi, M. Ghayour, S. Alivand, Small scale effect on the vibration of orthotropic plates embedded in an elastic medium and under biaxial in-plane pre-load via nonlocal elasticity theory, 2012.

[33] A. Farajpour, M. Danesh, M. Mohammadi, Buckling analysis of variable thickness nanoplates using nonlocal continuum mechanics, *Physica E: Low-dimensional Systems and Nanostructures*, Vol. 44, No. 3, pp. 719-727, 2011.

[34] N. Ghayour, A. Sedaghat, M. Mohammadi, Wave propagation approach to fluid filled submerged visco-elastic finite cylindrical shells, 2011.

[35] H. Moosavi, M. Mohammadi, A. Farajpour, S. Shahidi, Vibration analysis of nanorings using nonlocal continuum mechanics and shear deformable ring theory, *Physica E: Low-dimensional Systems and Nanostructures*, Vol. 44, No. 1, pp. 135-140, 2011.

[36] M. Mohammadi, M. Ghayour, A. Farajpour, Analysis of free vibration sector plate based on elastic medium by using new version of differential quadrature method, *Journal of Simulation and Analysis of Novel Technologies in Mechanical Engineering*, Vol. 3, No. 2, pp. 47-56, 2010.

[37] M. Goodarzi, M. Mohammadi, M. Khooran, F. Saadi, Thermo-mechanical vibration analysis of FG circular and annular nanoplate based on the visco-pasternak foundation, *Journal of Solid Mechanics*, Vol. 8, No. 4, pp. 788-805, 2016.

[38] C. Rumsey, Turbulence Modeling Resource. NASA Langley Research Center, Hampton, VA, 2020.

[39] B. Launder, Simulation and modeling of turbulent flows, *ICASE/Larc Series in Computational Science and Engineering*, Vol. 109, 1996.

[40] P. Spalart, S. Allmaras, A one-equation turbulence model for aerodynamic flows, in *Proceeding of*, 439.

[41] F. R. Menter, Two-equation eddy-viscosity turbulence models for engineering applications, *AIAA journal*, Vol. 32, No. 8, pp. 1598-1605, 1994.

[42] S. Azad, A. Riasi, H. Mahmoodi Darian, H. Amiri Moghadam, Parametric study of a viscoelastic RANS turbulence model in the fully developed channel flow, *Journal of Computational Applied Mechanics*, Vol. 48, No. 1, pp. 65-74, 2017.

[43] M. Ghasemian, A. Nejat, Aerodynamic Noise computation of the flow field around NACA 0012 airfoil using large eddy simulation and acoustic analogy, *Journal of Computational Applied Mechanics*, Vol. 46, No. 1, pp. 41-50, 2015.

[44] Z. Malikov, Mathematical model of turbulence based on the dynamics of two fluids, *Applied Mathematical Modelling*, Vol. 82, pp. 409-436, 2020.

[45] Z. Malikov, M. Madaliev, Numerical simulation of two-phase flow in a centrifugal separator, *Fluid Dynamics*, Vol. 55, No. 8, pp. 1012-1028, 2020.

[46] D. Spalding, CHEMICAL-REACTION IN TURBULENT FLUIDS, *Physicochemical Hydrodynamics*, Vol. 4, No. 4, pp. 323-336, 1983.

[47] B. E. Launder, G. J. Reece, W. Rodi, Progress in the development of a Reynolds-stress turbulence closure, *Journal of fluid mechanics*, Vol. 68, No. 3, pp. 537-566, 1975.

[48] C. Hirsch, Numerical computation of internal and external flows. Vol. 2-Computational Methods for Inviscid and Viscous Flows, *Chichester*, 1990.

[49] J. Delville, S. Bellin, J. Garem, J. Bonnet, *Analysis of structures in a turbulent, plane mixing layer by use of a pseudo flow visualization method based on hot-wire anemometry*, in: *Advances in Turbulence 2*, Eds., pp. 251-256: Springer, 1989.

[50] З. Маликов, М. Мадалиев, Численное моделирование течения в плоском внезапно расширяющемся канале на основе новой двужидкостной модели турбулентности, *Вестник Московского государственного технического университета им. НЭ Баумана. Серия «Естественные науки»*, No. 4 (97), pp. 24-39, 2021.

[51] D. W. Peaceman, J. Rachford, Henry H, The numerical solution of parabolic and elliptic differential equations, *Journal of the Society for industrial and Applied Mathematics*, Vol. 3, No. 1, pp. 28-41, 1955.

[52] S. V. Patankar, 2018, *Numerical heat transfer and fluid flow*, CRC press,